



## Research paper

## Microwave plasma modelling for thick diamond deposition on III-nitrides

Jerome A. Cuenca<sup>a</sup> ,\* , Ali Al-Moathin<sup>b</sup> , Menno J. Kappers<sup>c</sup> , Soumen Mandal<sup>a</sup> ,  
 Martin Kuball<sup>d</sup> , Rachel A. Oliver<sup>c</sup> , Chong Li<sup>b</sup> , Oliver A. Williams<sup>a</sup> 

<sup>a</sup> School of Physics and Astronomy, Cardiff University, Cardiff, CF24 3AA, United Kingdom

<sup>b</sup> James Watt School of Engineering, University of Glasgow, Glasgow, G12 8QQ, United Kingdom

<sup>c</sup> Cambridge Centre for Gallium Nitride, University of Cambridge, Cambridge, CB3 0FS, United Kingdom

<sup>d</sup> Center for Device Thermography and Reliability, University of Bristol, Bristol, BS8 1TL, United Kingdom



## ARTICLE INFO

## Keywords:

Diamond  
 Microwave plasma model  
 Chemical vapour deposition  
 Gallium nitride  
 Aluminium gallium nitride

## ABSTRACT

Microwave plasma chemical vapour deposition (MP-CVD) of thick polycrystalline diamond (PCD) ( $t > 100 \mu\text{m}$ ) is demonstrated on flipped III-nitrides (III-N)/gallium nitride (GaN) on Si using a sample holder designed using iterative microwave plasma modelling. The damage of flipped III-N/GaN in  $\text{H}_2$  plasma is due to superheating, caused by expansion of voids in the bonding layer from the flipping process and etching of the III-N/GaN film at an onset of above  $\sim 720^\circ\text{C}$ . This study demonstrates that holders with a tapered base allow rapid sample cooling ( $T \sim 669^\circ\text{C}$ ) to mitigate damage in a reactive hydrogen plasma at high-power and pressure. This holder enables, high quality thick PCD deposition and demonstrates the importance of microwave plasma modelling for cost-effective iteration of sample holder/susceptor design for temperature regulation.

## 1. Introduction

Heterogeneous integration of high thermal conductivity diamond on III-nitrides (III-N), such as aluminium nitride (AlN), aluminium gallium nitride (AlGaN) and gallium nitride (GaN) is a key challenge for miniaturisation and increased reliability of high-power GaN-on-Diamond based devices [1,2]. However, GaN-on-Diamond still remains a challenge with both wafer bonding and direct chemical vapour deposition (CVD). Wafer bonding with surface activation [3,4] or wet chemistry [5] has been shown over small area but requires strict cleanliness and roughness across both surfaces. Direct CVD is currently the only viable approach for larger area, with either hot-filament (HF-CVD) or microwave plasma (MP-CVD). The two most investigated limitations with CVD is that (1) GaN is not known to form a stable carbide [6] and requires an interlayer which introduces a finite thermal resistance (AlN, AlGaN, SiN) and (2) the differences in thermal expansion coefficient generates thermal stresses and creates adhesion challenges [7,8]. Although, for (1) interlayer thermal resistance can be low using the right thickness [9,10] and for (2) even with large thermal stresses ( $\sim 1 \text{ GPa}$ ), adhesion has been demonstrated [8,11], making CVD a viable route for large area GaN-on-Diamond.

However, the most severe challenge that is seldom addressed is that GaN is known to decompose in  $\text{H}_2$  rich atmospheres at typical CVD temperatures ( $T \sim 800$  to  $1000^\circ\text{C}$ ) and pressures ( $> 133 \text{ mbar}$ ) [12]. This is due to  $\text{H}_2$  reacting with GaN to create liquid Ga and  $\text{NH}_3$  [13].

Koukitsu et al. also showed that the decomposition rate of both the Ga and N polar faces (at atmosphere) reduces by almost an order of magnitude when  $T$  is reduced from  $\sim 850$  to  $\sim 700^\circ\text{C}$  [14]. Others show an onset of GaN decomposition at  $720$  to  $760^\circ\text{C}$  [13,15,16]. Low  $T$  MP-CVD therefore reduces the risk of decomposition, achieved by reducing the microwave power ( $< 3.5 \text{ kW}$ ) and pressure ( $< 80 \text{ mbar}$ ) or microwave power density (MWPD). However, low MWPD methods produce nano-crystalline films of low thermal conductivity ( $< 1000 \text{ W/m K}$ ) due to phonon scattering from the grain boundaries and non-diamond carbon (NDC), identifiable using Raman Spectroscopy [17,18]. Growth rates are also low ( $< 500 \text{ nm/h}$ ) due to a reduced H-radical density which is responsible for H surface abstraction, generation of carbon growth species ( $\text{H} + \text{CH}_4 \rightarrow \text{CH}_3 + \text{H}_2$ ) and suppression of NDC [19,20]. NDC is preferentially etched due to the increased penetration of energetic H atoms ( $\sim 1 \text{ eV}$ ) through  $\text{sp}^2$  carbon layers when compared to  $\text{sp}^3$  carbon [21]. Thus, low MWPD alone is not viable for GaN-on-Diamond.

A high-quality diamond/SiN/GaN interface has been shown by Malakoutian et al. using a small but high MPWD plasma ( $1.6 \text{ kW}$  at  $80 \text{ mbar}$ ) [10]. Previous work on small millimetre diamond/III-N/GaN membranes also shows a high MWPD approach ( $> 5 \text{ kW}$  at  $160 \text{ mbar}$ ), at low substrate temperatures of  $720$  to  $750^\circ\text{C}$ . Therefore, the current challenge is to optimise recipes for high MWPD at low  $T$  over larger areas.

Plasma modelling has emerged as a cost-effective optimisation tool for MP-CVD, providing fundamental understanding of the electron and

\* Corresponding author.

E-mail address: [cuencaj@cardiff.ac.uk](mailto:cuencaj@cardiff.ac.uk) (J.A. Cuenca).

<https://doi.org/10.1016/j.carbon.2025.120349>

Received 30 December 2024; Received in revised form 11 April 2025; Accepted 16 April 2025

Available online 30 April 2025

0008-6223/© 2025 The Authors. Published by Elsevier Ltd. This is an open access article under the CC BY license (<http://creativecommons.org/licenses/by/4.0/>).

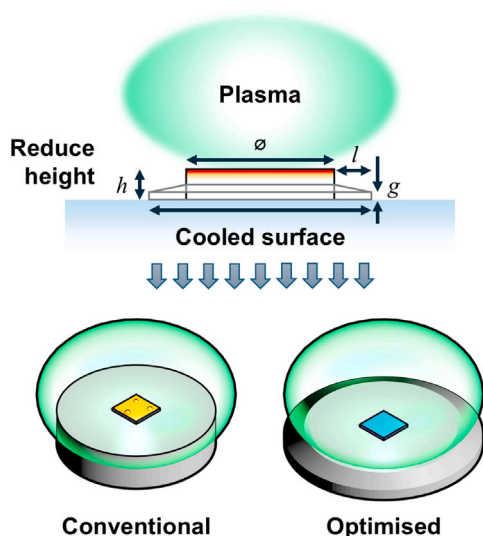


Fig. 1. Example schematic of conventional cylindrical holder and optimised tapered holder for MP-CVD.

H-radical number densities and gas temperatures to determine where diamond is deposited in the various reactor topologies. Common reactor types include bell-jar [22,23] cylindrical [24–26], clamshell [27,28] and ellipsoidal [29,30], each exhibiting different plasma distributions. In recent years, modelling has been used for understanding gas mixtures [31–33], deposition homogeneity over small to large areas [28, 34,35] and designing completely new systems [36,37]. In the context of GaN-on-Diamond, computational methods can be used to optimise growth temperatures.

In this work, we use an existing microwave plasma modelling method [28] to cost-effectively design a MP-CVD holder to operate at high MWPD whilst also mitigating damage of flipped III-N/GaN films by reducing the temperature. This work demonstrates that by using this holder thick ( $t > 100 \mu\text{m}$ ) high quality PCD can be grown at almost double the growth rate with no visible damage.

## 2. Design

Substrate holder design is a common method for regulating temperatures where recessed holders have been shown to optimise single crystal growth [38,39] and optimal heights can be found for polycrystalline growth [28]. The substrate temperature is a result of the competing forces between the high gas temperature of the plasma ( $>2000 \text{ }^\circ\text{C}$ ) and the cooling power of the reactor stage. Fig. 1 shows the concept for a tapered holder design with increased cooling power for deposition on substrates that fit on a  $\phi = 40 \text{ mm}$  surface. The perimeter of the sample holder is imperative for focusing the plasma over a small area for fast diamond growth. In comparison to a typical cylindrical substrate holder, a lower holder moves the sample away from the high temperature  $\text{H}_2$  plasma while the tapered base increases the cooling power resulting in a further reduction in temperature.

The extent to which the holder can taper (defined as  $l$ ) is limited by manufacturing restraints and Mo rod size. Machining the Mo rod requires a minimum rod grip, giving a taper base height of 3 mm. Through iterative plasma modelling, the cooled surface area of this holder can be varied to reduce the temperature and reduce III-N/GaN damage, where a base model with no tapering ( $\phi = 40 \text{ mm}$ ,  $h = 10 \text{ mm}$ ,  $l = 0 \text{ mm}$ , denoted “H10”) is swept through practical manufacturing limits of a  $\phi = 50 \text{ mm}$  Mo rod ( $h_{\text{lim}} = 5\text{--}10 \text{ mm}$ ,  $l_{\text{lim}} = 0\text{--}5 \text{ mm}$ ) towards “H05T5”.

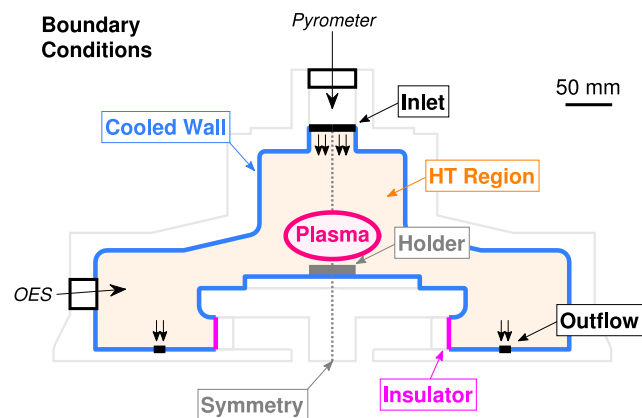


Fig. 2. 2D axisymmetric model of MP-CVD reactor with heat transfer boundary conditions. “Inlet” and “Outlet” denote gas flow continuity, the “HT region” denotes a domain of a  $\text{H}_2$  gas during discharge, “Holder” denotes a solid region of Mo, “Cooled Walls” denote the cooling flux, “Insulator” denotes an un-cooled wall and the ellipsoid labelled “Plasma” denotes the approximate location of the heat source. Pyrometer and OES locations are also shown for experimental reference.

## 3. Modelling

### 3.1. Method

Finite element modelling (FEM) is the process of dividing a continuous space into discrete domains and nodes with governing physics defined by partial differential equations (PDE). Full details of the model are given in previous work [28]. In brief, this work uses a 2D axisymmetric model of a Carat Systems CTS6U reactor at 5 kW at 160 mbar with an inlet gas flow of 300 sccm. This model uses a 3-step process: electromagnetic eigenfrequency solution, a frequency transient coupled electromagnetic/plasma fluid solution and a coupled heat transfer/laminar flow solution. The eigenfrequency step determines if the sample holder modifications significantly perturb the frequency of the reactor outside of the operational bandwidth. The electromagnetic/plasma fluid step calculates the applied E-field at a given power and uses energy dependent electron-species impact reactions to generate the plasma species including electrons ( $e$ ), neutral  $\text{H}_2$ ,  $\text{H}_2^+$  ions, H-radicals and excited  $\text{H}_2^*$  species. This step is also important to ensure that the plasma is located on the reactor stage. The heat transfer step uses the calculated microwave power deposited into the plasma as heat source in a COMSOL defined  $\text{H}_2$  gas domain whilst competing cooling flux boundary conditions allow the model to reach a temperature equilibrium. Since the focal point of this study is temperature reduction, only the heat transfer physics will be discussed and we refer the reader to previous work for the details on the full model [28].

A simplified schematic of the boundary conditions is shown in Fig. 2. In this step, both the competing gas heating and cooling forces in the MP-CVD reactor can be described in FEM using steady state heat transfer PDE’s:

$$\rho C_p \mathbf{u} \cdot \nabla T + \nabla \cdot \mathbf{q} = Q \quad (1)$$

where  $\rho$  is the medium density,  $\mathbf{u}$  is the velocity field,  $C_p$  is the heat capacity at constant pressure,  $T$  is the temperature,  $\mathbf{q} = -k\nabla T$  is the local heat flux density,  $k$  is the thermal conductivity and  $Q$  is a heat source/sink. This PDE is used for both the gas (orange region in Fig. 2) and also the solid Mo sample holder (solid grey region in Fig. 2) where the first term with gas flow velocity is ignored. At the extremities of the reactor, wall boundaries are modelled as cooling fluxes normal to the surface (blue lines in Fig. 2), described by:

$$-\mathbf{n} \cdot \mathbf{q} = h_{\text{cool}}(T_{\text{ext}} - T) \quad (2)$$

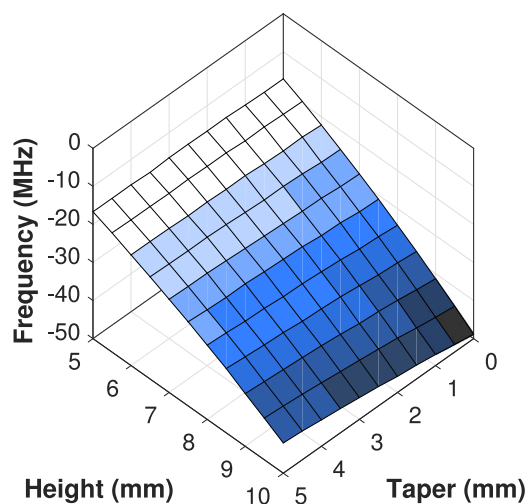


Fig. 3. FEM eigenfrequency results for a cylindrical sample holder ( $\varnothing = 40$  mm) with varying height and tapering.

where  $h_{\text{cool}}$  is the heat transfer coefficient and  $T_{\text{ext}} = 20$  °C is the reference external temperature.  $h_{\text{cool}}$  is associated with the reactor cooling and is determined through experiment using varying sample holder heights [28]. In this way, the temperature at the top surface of the Mo holder varies. It must be noted that the stage piece has been modified compared to previous work. Insulator, inlets and outflows are modelled where  $-\mathbf{n} \cdot \mathbf{q} = 0$ .

### 3.2. Eigenfrequency results

The eigenfrequency results for varying the cylindrical holder height and tapering are shown in Fig. 3. The  $h = 10$  mm standard holder perturbs the reactor by  $\Delta f \approx -50$  MHz than its designed frequency of 2.45 GHz. Assuming the modelled outer boundaries of the microwave cavity to be of high conductivity metals ( $\sigma > 1 \times 10^6$  S/m), this evaluates a modelled quality ( $Q$ ) factor  $> 10^4$  or an equivalent operating half power bandwidth ( $\Delta BW$ ) at 2.45 GHz of only  $\Delta BW = 245$  kHz. At first, this seems problematic, however in reality the output spectra of magnetron technology also spans  $\pm 50$  MHz range, and is indeed even more controllable for solid state technology [40].

### 3.3. Field distributions

Field distributions are shown in Fig. 4 for the eigenfrequency, plasma fluid and heat transfer solutions for the conventional holder (H10) and the proposed tapered holder (H05T5) with and without the sample present. The eigenfrequency solution shows a characteristic  $TM_{011}$  mode in the central region of the reactor. For a  $TM_{011}$  mode, a co-sinusoidal standing wave on the axis means that a plasma is equally likely to occur at either the top or the bottom, however, in this reactor, the presence of the top waveguide mitigates the formation of a high E-field region. In the absence of any holder, the  $z$  radial component of the E-field distribution on the surface of the stage follows a Bessel function of the first kind  $E_z(r) = J_0(r)$ , however the holder edges create a discontinuity causing the E-field to focus here, making the holder critical to maintaining the plasma on the stage. With lower holders, this effect is less profound. The plasma solution shows that the electron density is focused on the top of the holder. The conventional H10 holder pulls the plasma away from the central region due to the E-field focusing effect, resulting in accelerated reaction rates on the edges of the sample. At lower heights, the plasma maximum reverts to the centre of the holder. The heat solution shows that the gas temperatures reach in excess of 3000 K in the core of the plasma, with lower holders

allowing the core to expand; a greater holder perturbation results in a cooler gas. Laminar gas flow solutions show minimal difference as the sample holder is lowered.

Line scans on the surface of the sample holder are shown in Fig. 5 for E-field, electron density, H-radical density and temperature. Fig. 5(a) shows a flat E-field distribution with a focusing effect at the edges of the holder and sample. The overall E-field intensity also decreases with a sample present due to its flat orientation perpendicular to the E-field, thus creating field depolarisation. The plasma electron density distribution in Fig. 5(b) without a sample shows a relatively uniform density in the centre of  $n_e \approx 0.6 \times 10^{14} \text{ m}^{-3}$ , with heavily concentrated edge focusing due to the E-field focusing effect. A lower sample holder mitigates this edge effect, bringing the plasma into its original ellipsoidal profile in the centre and increasing the central density by  $4.5\times$  to  $n_e \approx 2.7 \times 10^{14} \text{ m}^{-3}$ . With the sample present, the electron density over the sample increases almost  $2\times$ , and the profile becomes flatter with lower height and tapering. Tapering also redistributes point focusing on the sample holder to the edge and base of the tapered holder. A similar distribution is noted for the H radical density since, as in numerous other modelling studies such as Lombardi et al. generation mechanisms of H radicals is due to  $e+\text{H}_2 \rightarrow e+2\text{H}$  reactions [41,42]. Although, the increase is only  $1.5\times$  without and  $1.3\times$  with a sample. The most notable result is that the temperature is significantly higher for H10, with a non-homogeneous temperature distribution rising from  $\sim 846$  °C in the centre to  $\sim 924$  °C at the edge. With a sample the central temperature increases by  $\sim 20$  °C. Reducing the holder height significantly reduces the holder perturbation and central temperature, while tapering reduces this further to  $\sim 637$  °C where a hump profile in the centre of the holder appears.

## 4. Experimental method

The representative III-N/GaN/Si samples used in this study were  $17 \times 17$  mm squares diced from a flipped 6" AlGaIn/GaN on Si wafer deposited using metalorganic vapour phase epitaxy (MOVPE). The III-N/GaN stack consisted of an AlN nucleation layer, graded AlGaIn strain management layer, GaN buffer layer, AlGaIn etch-stop layer, and a typical device layer structure consisting of a GaN channel, an AlN exclusion layer, an AlGaIn barrier layer and a GaN cap layer. This III-N/GaN stack represents a typical GaN-on-Si structure in the context of device applications. The stack was bonded to a sacrificial silicon/spin on glass (Si-SOG) handle wafer (Akash Systems) and diced to  $17 \times 17$  mm. The original Si substrate was then removed and the AlN nucleation and AlGaIn strain management layers were dry etched up to the AlGaIn etch-stop layer using a two stage inductively coupled plasma (ICP) recipe with in-situ interferometry monitoring [11]. In the first stage, a non-selective  $\text{Cl}_2/\text{Ar}$  ICP etch allowed a high etch rate removal of the AlN nucleation layer the AlGaIn strain management layer and the majority of the GaN buffer layer. In the second stage, the process was switched to a  $\text{Cl}_2/\text{O}_2/\text{N}_2$  GaN selective etch (over AlGaIn, selectivity  $x < 0.3$ ) to remove the remaining GaN buffer until the N-polar AlGaIn face is exposed for diamond growth. These samples were cleaned in solvents (isopropyl alcohol) and seeded using hydrogen terminated seeds in an ultrasonic nanodiamond colloid process [20]. The samples were then rinsed in deionised water, dried with compressed air and positioned on the sample holder inside the reactor.

MP-CVD deposition trials on III-N/GaN on Si were conducted using a clamshell style reactor. A 50 mm diameter Mo rod was used to produce the conventional 10 mm tall 40 mm diameter cylindrical (H10) holder and the newly optimised tapered sample holder (H05T5). All MP-CVD experiments were carried out using a standard  $\text{CH}_4/\text{H}_2$  gas mixture ( $\text{CH}_4$  at 3%, 300 sccm) and a microwave power ( $P$ ) and pressure ( $p$ ) of up to 5 kW at 160 mbar. First, damage trials are presented on both holders to determine the upper temperature limit for flipped III-N/GaN by ramping to high MWPD. Second, a sample was held at conditions just above the damage limit to observe the damage evolution

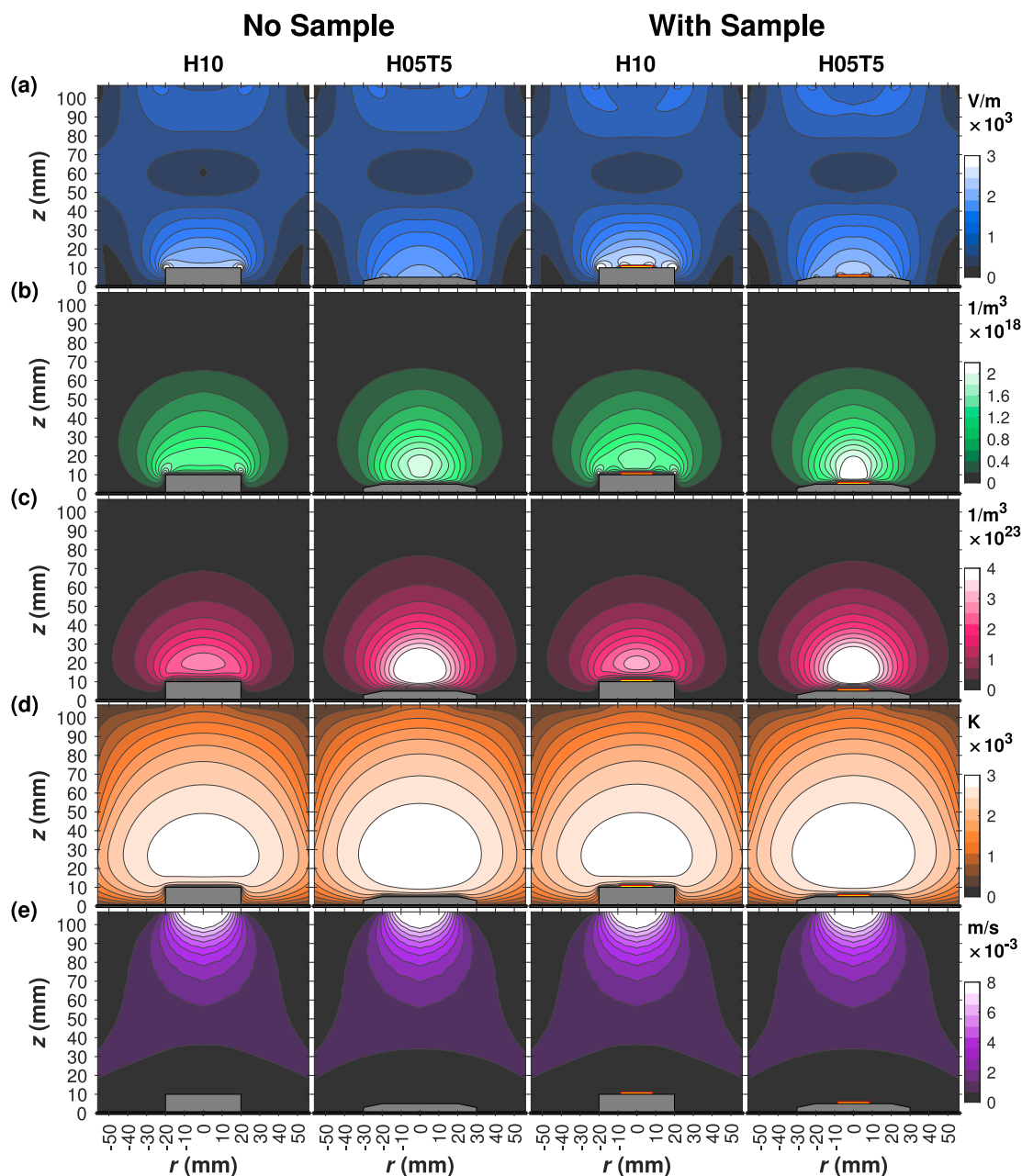


Fig. 4. FEM distributions of cylindrical and tapered holders at 5 kW and 160 mbar. Distributions shown are the (a) eigenfrequency E-Field, (b) plasma fluid electron density, (c) plasma H-radical density, (d) gas temperature and (e) laminar flow velocity fields. The red and yellow rectangle denotes a  $17 \times 1$  mm Si sample.

of the III-N/GaN film. Finally, thick diamond deposition was carried out on both holders; total duration of  $\sim 5$  days, (duration in  $\text{CH}_4/\text{H}_2$   $d \approx 96$  h) with an empty reactor cleaning intermission at the 48 h point ( $\text{O}_2/\text{H}_2$  at 3% for 24 h). Sample failures were stopped immediately. The substrate temperature was monitored from the top window using a Williamson dual wavelength pyrometer (DWF-24-36C), while in-situ images were obtained using an Apple iPhone 12 mini. Due to the optical interference from the III-N/GaN stack and emissions from glowing damage, ex-situ pyrometry measurements of dummy unseeded silicon samples of the same size were used for temperature reference in the damage trials. Samples were characterised using Raman Spectroscopy with a Horiba LabRAM HR Evolution with a grating of 18001/mm from 200 to  $1800 \text{ cm}^{-1}$ . For damage trials, a blue/cyan laser ( $\lambda = 473 \text{ nm}$ ,  $20\times$  objective) was used for sensitivity to GaN signatures, and for growth trials a green laser ( $\lambda = 532 \text{ nm}$ ,  $10\times$  objective) was used to allow for sensitivity to both  $\text{sp}^3$  and  $\text{sp}^2/\text{NDC}$ . Optical emission spectra

(OES) was obtained by aiming an optical fibre at the plasma from the side window as shown in Fig. 2 using an Ocean Optics 2000 series spectrometer. Side port windows were thoroughly cleaned with water and isopropyl alcohol before MP-CVD trials as they are prone to carbon deposition which restricts the observed emission intensity.

## 5. Experiment

### 5.1. Damage limit

Fig. 6 shows images of the typical MP-CVD damage phenomenon that occurs on flipped III-N/GaN samples during ramping up to high MWPD. For H10, the sample remains undamaged at  $< 4.5 \text{ kW}$ , 107 mbar ( $< 720 \text{ }^\circ\text{C}$ ). Above this threshold, orange spots and globules appear on both the edge and centre of the sample, see supplementary data for additional cases. A practical damage limit is thus defined as  $\sim 4 \text{ kW}$  at

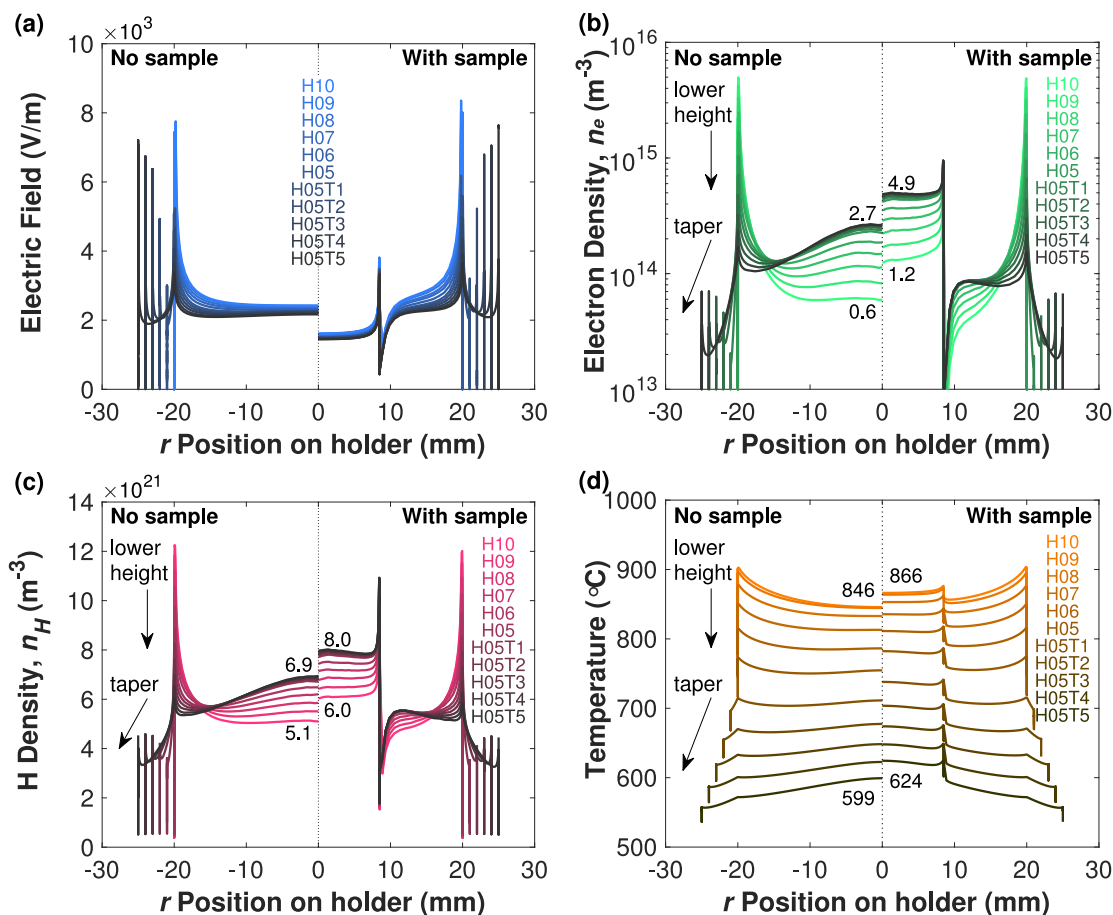


Fig. 5. FEM line scan data of sample holder surface with and without sample (a) eigenfrequency E-field (b) plasma electron density (c) plasma H radical density and (d) temperature for a conventional cylindrical holder (H10) with incremental modifications towards a tapered holder (H05T5) at 5 kW at 160 mbar. Annotations show value at  $r = 0$ .

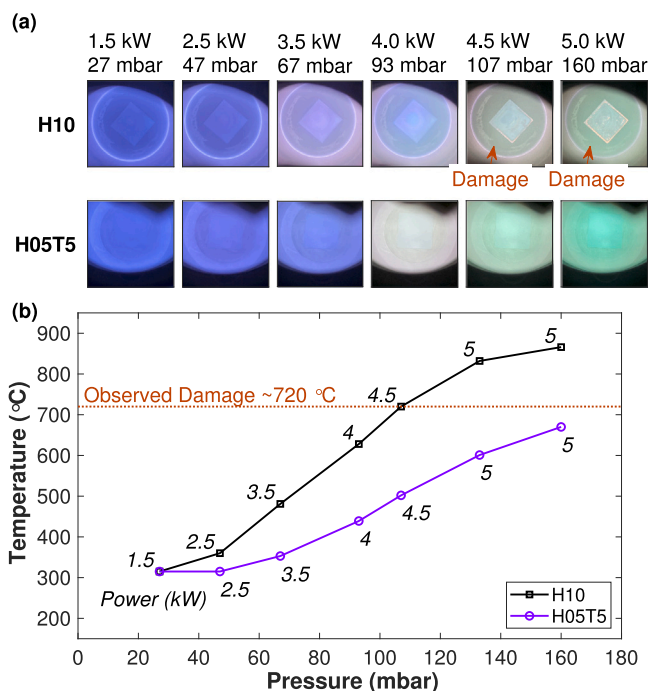


Fig. 6. Damage ramping trials, (a) Photographs of a flipped III-N/GaN on Si sample during MP-CVD at various MWPD from just after plasma ignition and stabilisation (1.5 kW at 27 mbar) to very high MPWD (5 kW at 160 mbar) and (b) pyrometry data of a Si sample at the same conditions to infer III-N/GaN substrate temperature.

93 mbar on H10. For H05T5 however, the sample shows no signs of damage even towards 5 kW at 160 mbar at a temperature of ~669 °C.

Fig. 7 shows microscopy and Raman data for a III-N/GaN on Si sample at just above the damage threshold (4.5 kW 120 mbar). Fig. 7(a) shows the in-situ formation of superheating hotspots, where Fig. 7(b-c) shows that these are bulges, some of which have exploded and delaminated the diamond/III-N/GaN film. The Raman spectra in Fig. 7(d) shows characteristic peaks for the Si substrate (first-order ~520 cm<sup>-1</sup>, second-order 900 to 1000 cm<sup>-1</sup> [43]) and the III-N/GaN structure (E<sub>2</sub> mode ~567 cm<sup>-1</sup> and A<sub>1</sub> mode ~734 cm<sup>-1</sup> of wurtzite GaN [44]). The absence of the AlN E<sub>2</sub> (~657 cm<sup>-1</sup>) and A<sub>1</sub> (~890 cm<sup>-1</sup>) modes is due to the small AlN thickness and relatively low Al content in the AlGaN strain management layer. A diamond peak ( $\omega_0 \approx 1333$  cm<sup>-1</sup>) with a full-width at half-maximum (FWHM) of  $\gamma \approx 6$  cm<sup>-1</sup> is shown with accompanying G (1580 cm<sup>-1</sup>) and D'-bands (1620 cm<sup>-1</sup>), associated with the bond stretching mode of sp<sup>2</sup> carbon and clusters of C=C chains in sp<sup>3</sup> carbon rich materials, respectively [45,46]. Additionally two bands at ~1100 cm<sup>-1</sup> and ~1470 cm<sup>-1</sup> are attributed to concentrations of transpolyacetylene (TPA) in the grain boundaries [47]. The films imply good crystalline quality however a concentration of NDC impurities in the film. In the damaged region, there are no III-N/GaN or carbon signatures.

### 5.2. Diamond growth

Two growth trials were carried out at high MWPD on both holders and one at lower MWPD using H10. A summary of the growth trial parameters and measured rates are given in Table 1. Fig. 8(a) shows the pyrometry traces for all 3 growths. At the start, the characteristic

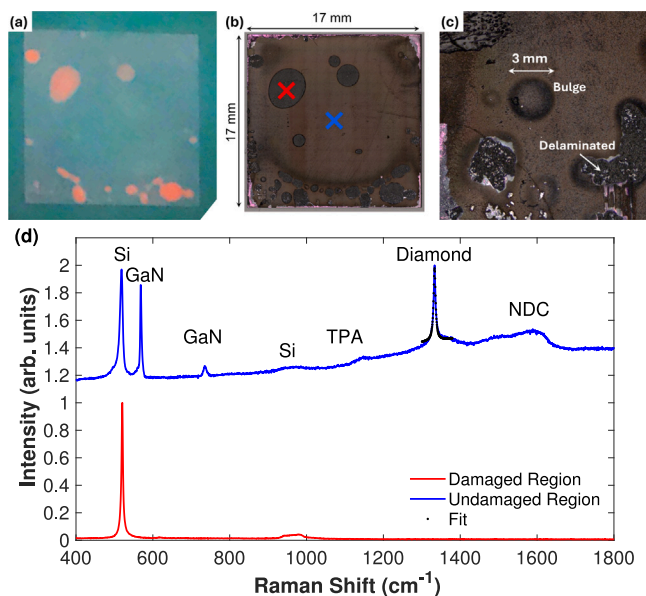


Fig. 7. Damage trials held at 4.5 kW at 120 mbar, (a) photographs of a damaged flipped III-N/GaN on Si during MP-CVD, (b) subsequent stitched microscope images of the sample, (c) magnified view of bottom left corner and (d) Raman spectra at damaged and undamaged locations are marked by red and blue crosses, respectively. Dotted line shows a Lorentzian fit with a positive linear background ( $\frac{a}{\pi} \frac{\gamma}{(\omega - \omega_0)^2 + \gamma^2} + b\omega$ ), where  $a$  is an amplitude scalar,  $\gamma$  is the FWHM,  $\omega_0$  is the peak centre and  $b$  is an offset factor.

Table 1

Summary of diamond growth recipe parameters and metrics.

Holder	P kW	p mbar	T °C	Avg. Rate μm/h		t <sup>a</sup> μm	d h
				Step 1	Step 2		
H10	5	147	889	1.54	–	88	57
H10	4	93	680	0.33	1.05	66	96
H05T5	5	160	669	0.60	1.95	122	96

<sup>a</sup> Thickness as determined by the difference in mass before and after deposition.

optical interference oscillations are indicative of the coalescence and growth of a nanometre thin CVD diamond film [48]. As the film grows to 1–10 μm, the film roughness scatters the interference and reveals the apparent substrate temperature, those given in Table 1. Note that coalescence on H05T5 occurs much faster than on H10 at similar temperatures, implying a much faster growth rate in the first 24 h.

Fig. 8 (b–g) shows images of growth runs using both H10 and H05T5 holders at high MWPD. The images from the side port show the characteristic green ellipsoidal plasma glow. From the side and top, the plasma with H10 is clearly less bright when compared to H05T5. Additionally, the edges of H10 are much brighter than H05T5, with a greater purple emission caused by the holder field focusing effect that is evidently reduced for tapered holders. At the interface between the holder and the plasma, the sample grown on H10 is glowing orange, clearly in excess of ~800 °C, compared to H05T5 which remains visibly undamaged throughout the entire deposition process. This is best observed from side ports owing to the intense plasma emission. Orange super-heating spots begin to appear on the sample which ultimately destroys the III-N/GaN film. As deposition progresses, these super-heating patches become less visible and are covered in diamond although the resulting film was significantly damaged at 57 h and deformed upon cooling the sample to room temperature (not shown).

Fig. 9 shows the optical emission spectra from the side port of the reactor using the 2 holders. Emissions from the C<sub>2</sub> swan band (468, 516, 558 and 560 nm), CH radicals (431 nm) and the H-Balmer series (486 and 656 nm) are observed [49]. At an ignition MWPD of 1.5 kW at

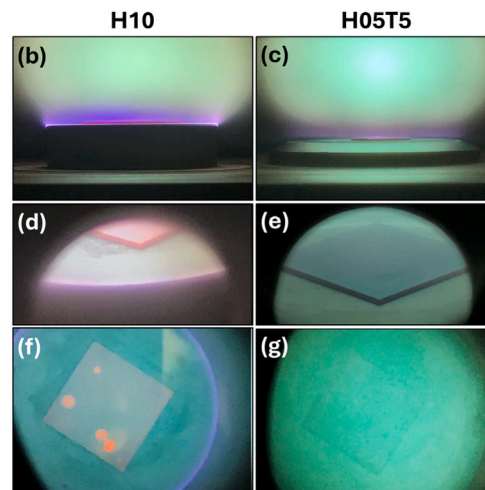
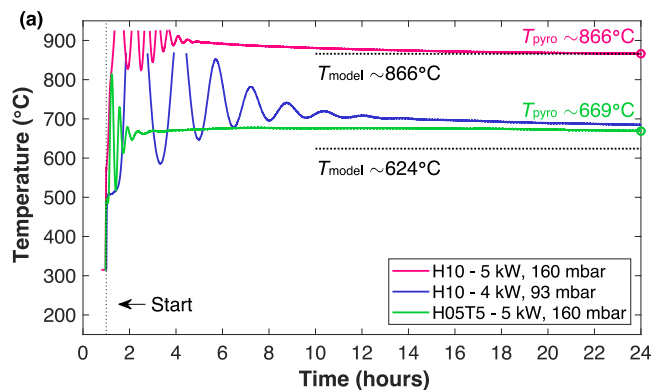


Fig. 8. (a) Pyrometry traces of the 3 growth trials and photographs of the plasma during high MWPD deposition from (b–c) side, (d–e) angled and (f–g) top window within the first 15 min. The contrast and brightness of image (f) has been adjusted for visibility of damage.

27 mbar, only the H-Balmer series is measurable for both holders, with broad bands from background nitrogen in the chamber. With increasing MWPD, the 385 nm CN/CH band emerges as well as the C<sub>2</sub> swan band, indicative of C<sub>2</sub> dimer production. C<sub>2</sub> dimer production is not the primary diamond growth species, however, the C<sub>2</sub> swan bands are an indication of a greater collision frequency with the CH<sub>4</sub> precursor and therefore CH<sub>3</sub> growth species which increases rate. The C<sub>2</sub> and H emissions have a higher intensity for H05T5 compared to H10. This is corroborated in the model where lower profile holders do not perturb the plasma core as much which reduces the H-radical density. Note that at similar substrate temperatures, 4 kW at 93 mbar on H10 and 5 kW at 160 mbar on H05T5, the C<sub>2</sub> emission is much lower at lower pressure, thus a lower growth rate is expected for the same CH<sub>4</sub>/H<sub>2</sub>.

### 5.3. Raman spectroscopy

Fig. 10(a) shows a stitched optical image and (b–c) mapped Raman spectroscopy for before MP-CVD on H05T5 (high MWPD). The starting sample shows a homogenous distribution of Si and III-N signatures. Fig. 10(d) shows a stitched optical image of the PCD film and (e–f) mapped Raman spectroscopy after MP-CVD. Raman mapping clearly demonstrates a first-order sp<sup>3</sup> carbon diamond peak at (1332±0.3 cm<sup>-1</sup>) with an average FWHM over the film of  $\gamma \approx 5 \pm 1$  cm<sup>-1</sup>. There is no detectable NDC band or G-band (1580 cm<sup>-1</sup>) or D'-band (1620 cm<sup>-1</sup>), implying high quality diamond. However, there is a band at ~1420 cm<sup>-1</sup> which is attributed to nitrogen vacancies (NV<sup>0</sup>) [37,50], either from the background N<sub>2</sub> in the reactor or etched from the N-polar

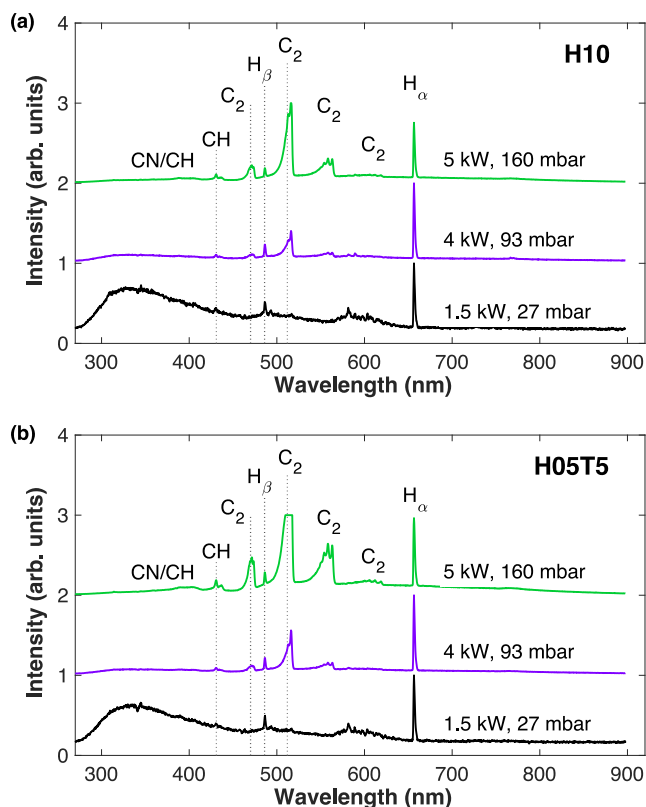


Fig. 9. OES Spectra taken at different MWPD using (a) H10 and (b) H05T5 holders. Spectra normalised to maximum.

surface. The first-order Si and E<sub>2</sub> GaN modes are clearly measurable through the  $t > 100 \mu\text{m}$  thick CVD diamond (as determined by mass). The GaN/Diamond intensity ratio (ratio of the  $567 \text{ cm}^{-1}$  peak over the  $1332 \text{ cm}^{-1}$ ) on the left-most edge it is immeasurable, likely due to diamond overgrowth. The variation in GaN/Diamond intensity is likely due to the distribution in electron and H-radical density as shown in the model, and thus a growth rate variation. The sample also appears to be positioned off centre as the GaN/Diamond intensity is generally lower towards the top left edge. The III-N/GaN film has a detectable  $>10 \times 10 \text{ mm}^2$  area that remains during deposition, thereby demonstrating that by simply altering the MP-CVD sample holder low temperature diamond growth at high MWPD is a possible route for overcoming III-N/GaN damage over larger area. Fig. 10 (g-i) shows optical images of the MP-CVD diamond film grown on H05T5 with various objectives. The grain sizes are clearly of the order of  $>20 \mu\text{m}$ , sufficiently larger than  $10 \mu\text{m}$  to realise high thermal conductivity PCD ( $\sim 1000 \text{ W/m K}$ ) [51].

Fig. 11(a) shows a stitched optical image and (b-c) mapped Raman spectroscopy of the sample before MP-CVD on H10 (medium MWPD). Similar to Fig. 10(a), the sample shows the same characteristic Si and III-N peaks, however the GaN/Si ratio is far more prominent at almost a 1:1 ratio, implying a slightly different composition or thicker AlGaIn stack. After deposition the first-order Si and E<sub>2</sub> GaN modes are again measurable through the  $\sim 66 \mu\text{m}$  thick PCD film. However, the first-order sp<sup>3</sup> carbon diamond peak at  $(1332 \pm 0.3 \text{ cm}^{-1})$  has a larger average FWHM of  $\gamma \approx 8 \pm 3 \text{ cm}^{-1}$ , implicit of lower quality grains. The background photoluminescence is higher with some evidence of low intensity NDC bands. In general, Fig. 11 (g-i) shows a darker and lower quality film than the film grown on H05T5.

## 6. Discussion

This study demonstrates that lower temperature ( $<720 \text{ }^\circ\text{C}$ ) MP-CVD growth is necessary for deposition on flipped III-N/GaN on Si.

However, simply lowering the MWPD to avoid damage results in lower growth rates and lower quality diamond. In this study, higher MWPD is achievable with a  $\sim 2\times$  growth rate using a modelling optimised holder ( $\sim 1.95 \mu\text{m/hr}$ ). Although, at similar conditions, growth on Si is still much faster ( $\sim 3 \mu\text{m/hr}$  in 3% CH<sub>4</sub>/H<sub>2</sub> [46]). This is likely due to the higher temperatures that can be achieved on Si.

### 6.1. Superheating of GaN

One of the least reported phenomenons of MP-CVD on N-polar III-N/GaN films is the damage and super heating that is caused by such intense H<sub>2</sub> plasma process conditions needed for high-quality thermal grade diamond. This study identifies two damage routes to the superheating which are shown in Fig. 12.

First, we discuss the III-N/GaN-on-Si flipping process and its contribution to the superheating. GaN is typically MOVPE deposited as a Ga-polar film on Si or sapphire, or ‘device side’ up. Direct MP-CVD on this side thus introduces device fabrication challenges and so ideal practice is to bond the GaN-on-Si wafer to another Si handle to allow ‘flipping’ and etching of the original Si substrate to reveal the N-polar ‘non-device’ underside for diamond MP-CVD. However, if the bond is not perfectly seamless, voids of trapped gas can expand during the MP-CVD process resulting in the low thermal conductivity III-N/GaN film expanding, heating in the plasma and delaminating, see Fig. 12. This mechanism explains the bulges in the III-N/GaN film and why these orange superheating hotspots appear, see Fig. 7(a-c). This damage route is also less problematic at lower temperatures, and explains why damage was not observed at 669 to 680 °C but is significant at  $\sim 866 \text{ }^\circ\text{C}$ .

Next, we discuss the N-polar face in H<sub>2</sub>, which is known to be less stable than the Ga-polar face in H<sub>2</sub>. Koleske et al. showed that Ga droplet formation occurs on the surface of a III-N/GaN film in H<sub>2</sub> at 811 to 992 °C (at  $< 200 \text{ mbar}$ ) due to H etching of N to create NH<sub>3</sub> [12]. Yeh et al. also show that the Ga-polar surface is relatively stable at high temperatures in H<sub>2</sub> (at  $< 346 \text{ mbar}$ ), however, hydrogen still etches dislocations in the film and permeates to the N-polar faces to create deep cavities [52]. Thus, the exposed N-polar side is the most problematic and unstable face for MP-CVD. Although the N-polar face is covered and protected with diamond seeds, hydrogen can diffuse in-between the finite gaps before coalescence. Hydrogen then under-etches the film to create deep cavities that expand and cause delamination. As with GaN decomposition onset at 720 to 760 °C [15,16], this also explains why damage is not observed in the 669 to 680 °C MP-CVD growths, but is suddenly observed at  $>720 \text{ }^\circ\text{C}$ .

Finally, we discuss the model and contributions to the damage mechanisms. The model shows minimal difference in the E-field distribution between H10 and H05T5, implying microwave heating does not increase the risk damage. However, the field focusing causes the plasma to focus on the edges which slightly raises the temperature and damage risk, see Fig. 5(a). This also explains why damage appears to be more likely at the edges of the sample. Plasma focusing also increases H-radical production at the edges, where higher partial pressures of H<sub>2</sub> are known to increase decomposition [14]. However, the high H-radical density only seems problematic above  $\sim 720 \text{ }^\circ\text{C}$  and suggests that even higher power density plasmas can be used.

### 6.2. Temperature model discrepancy

The experimentally measured temperature is at least  $\sim 45 \text{ }^\circ\text{C}$  higher for H05T5 than modelling estimates. The initial model is experimentally calibrated to H10 and assumes a uniform cooling flux over the  $\phi = 40 \text{ mm}$  underside to match observed temperatures. This assumes that the holder and stage are in close contact. However, if the cooling flux is not radially uniform the cooling is not as effective. This may be due to the positioning of cooling pipes in the stage, a non planar stage or surface roughness under the holder. In this reactor, the stage

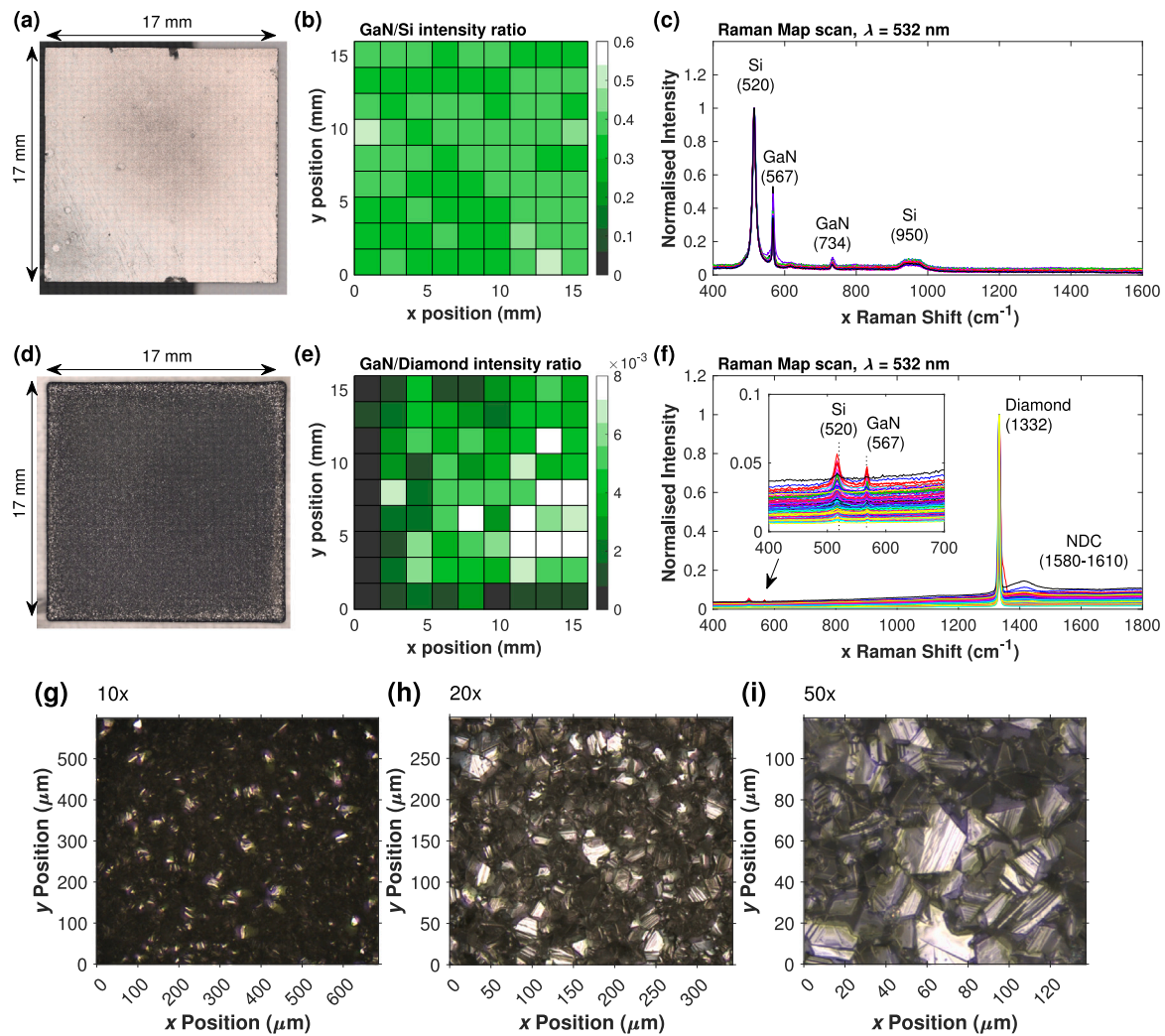


**Fig. 10.** Raman spectroscopy and optical microscopy of III-N/GaN sample grown using H05T5 at high MWPD, (a-c) before and (d-f) after >48 h MP-CVD deposition at 5 kW 160 mbar. Optical map images are stitched with a 10x objective. Raman maps show ratios of the GaN/Si and GaN/Diamond peak intensities while multiple coloured lines show multiple measurements on the sample overlaid. Inset shows magnified region for Si and III-N features. Optical images (h-i) show the film grown on H05T5 at varying magnification.

piece is a removable cylindrical Cu piece that is prone to warping over time ( $\varnothing = 150$  mm, height = 10 mm) and is therefore less planar, which we attribute as the primary systematic error. In the model, this can be calibrated by simulating a radial cooling flux underneath the holder that varies linearly by:

$$h_{\text{cool}}(r) = h_0 + \beta \left( \alpha - \frac{1}{r} \right) \quad (3)$$

where  $h_0$  is the uniform cooling flux,  $\beta$  is a linear scalar and  $\alpha$  is a constant offset. Fig. 13 shows the modified model for H05T5 with a radially varying cooling flux under the sample. Using H10 as a calibration,  $\alpha$  is adjusted for a given  $\beta$  to ensure a  $T = 866$  °C. The results show that as the cooling becomes increasingly less homogeneous, the central sample temperature begins to increase to experimentally observed values at  $\beta \approx 51$ .

Other sources of experimental error in temperature include the apparent spot size of the pyrometer (in this instance  $\varnothing \approx 22$  mm), however, modelling shows that the temperature is fairly uniform over this area. Such uniformity may be corroborated with scanning pyrometry methods although only if the spot size can be reduced for spatial resolution smaller than the sample size [53]. In the context of larger area deposition, a greater focus is needed on accurately modelling the spatial variation of the cooling flux on the stage, making in-situ spatial temperature measurements crucial for calibration. For current MP-CVD

reactors, scanning pyrometry is challenging since most viewports have small fields of view ( $\varnothing \approx 25$  mm) with considerable depth such that a cylindrical waveguide is formed with a cut-off frequency  $f_c > 2.45$  GHz to stop microwave leakage. Ultimately, this may require new reactors with multiple windows to view different parts of the wafer, or larger window positioning at points of low E-field (as can be determined using eigenfrequency E-field modelling). Alternatively, thermocouples embedded in the stage offer better insight, but requires significant cost. Alas, experimental model calibration is currently limited by low sample visibility reactors for pyrometry.

As cost-effective as experimentally calibrated modelling is at present, there are additional modelling errors which impact the temperature accuracy in holder design. Perfect assumptions are made on the material properties; for thermal conductivity in Eq. (1) standard COMSOL library material values are used for the Cu stage piece and Mo holder. In practice, oxides and deposited carbon reduces the thermal contact and the effective conduction between the holder and the stage is reduced. The presented model does not take this into account however, can be improved by creating material layers at the interface between the holder and stage and iterating the properties and holder radius accordingly to match experiment. Although this is also partly addressed using the above uniformity model, measurements of the materials used to build the reactor are likely to improve the model

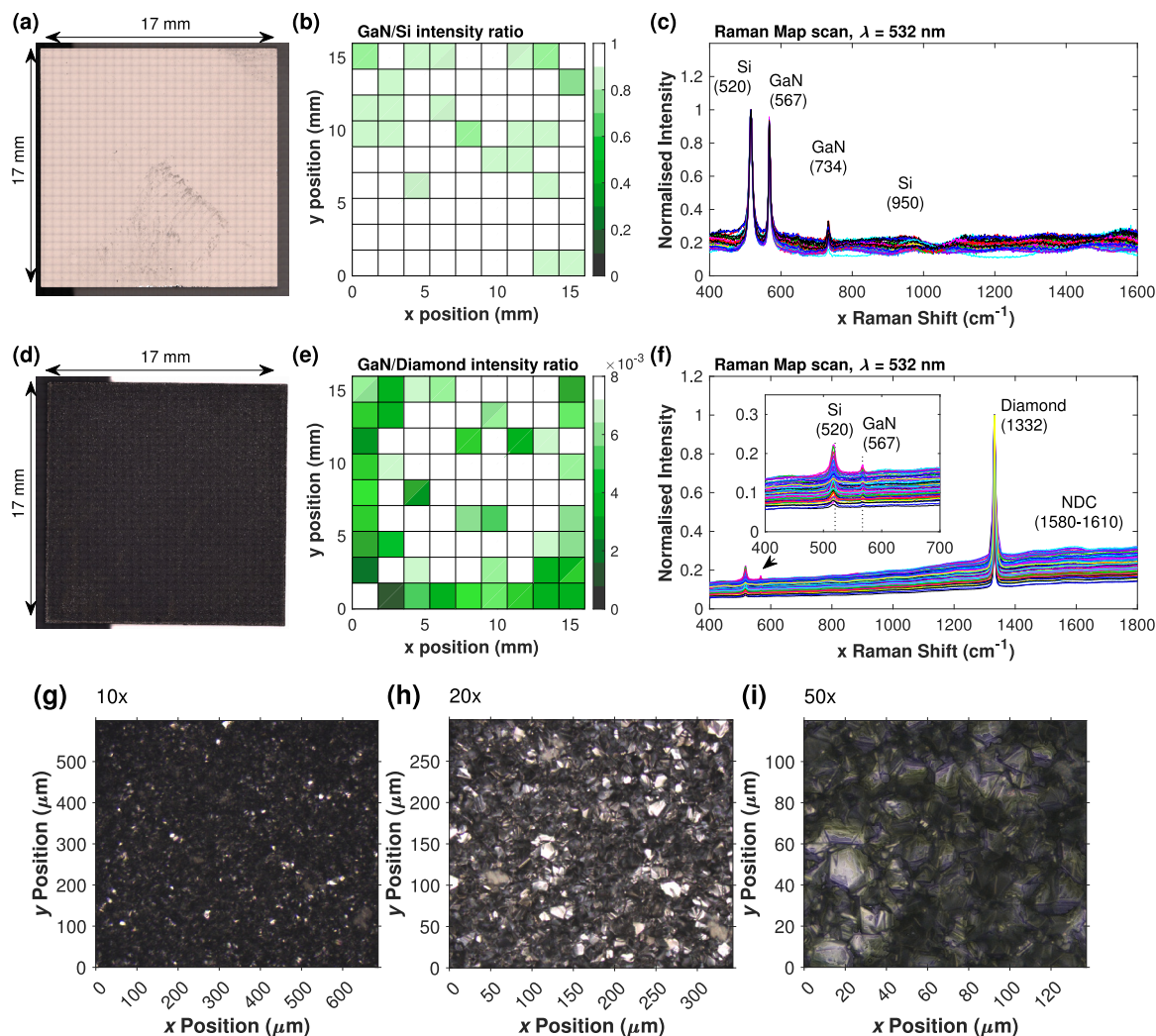


Fig. 11. Raman spectroscopy and optical microscopy of III-N/GaN sample grown using H10 at medium MWPD, (a-c) before and (d-f) after >48 h MP-CVD deposition at 5 kW 160 mbar. Optical map images are stitched with a 10x objective. Raman maps show ratios of the GaN/Si and GaN/Diamond peak intensities while multiple coloured lines show multiple measurements on the sample overlaid with background noise subtraction. Inset shows magnified region for Si and III-N features. Optical images (h-i) show the film grown on H05T5 at varying magnification.

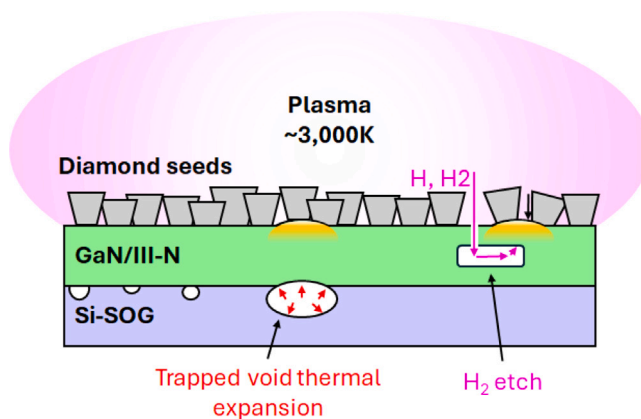


Fig. 12. Summary of flipped III-N/GaN damage mechanisms during MP-CVD.

accuracy. The modelled geometry of the reactor is also assumed correct and may have errors in tolerance, however, owing to the large length-scales compared to the holder size, errors in this are assumed negligible.

Finally gas chemistry may be too simplified with the absence of  $\text{CH}_4$ . However, as in previous work, this only results in a global shift in all temperatures [53]. Practically, variations in growth temperature of

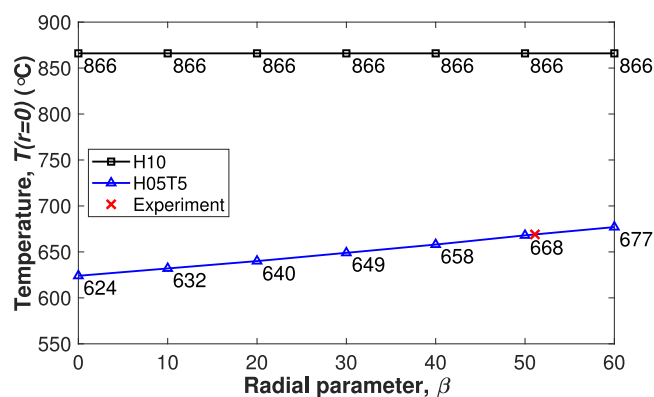


Fig. 13. Modelled temperature at the centre of the sample on H05T5 using a radially varying cooling flux.

the same samples can simply be due to placement, sample bow and cleanliness of the reactor.

### 6.3. Visibility through Raman

Although a thick polycrystalline diamond film with numerous grain boundaries exists on the flipped III-N/GaN epilayer structure on Si handle wafer, a surprising finding is that GaN and Si signals are still detectable underneath using Raman Spectroscopy. Although this has been reported for previous studies on Diamond-on-GaN membranes [8], this demonstrates that despite the poly-crystalline morphology, diamond grown by this low-temperature and high MWPD process results in films of lower than expected optical scattering, whereby low impurities allow for low extinction coefficients which is favourable for quantum-sensing applications [54]. III-N optical waveguide applications require low surface scattering losses from the substrate [55] and diamond grown in the proposed way may demonstrate prospects for higher power photonics applications, especially after polishing.

## 7. Conclusion

Thick MP-CVD diamond has been successfully deposited on a flipped III-N/GaN on Si handle wafer using a high MWPD plasma, for which the sample holder was designed using iterative microwave plasma modelling. Damage to the III-N/GaN is mitigated by rapid sample cooling with a tapered holder. High quality CVD films (as determined by Raman Spectroscopy) have been demonstrated owing to the high H-radical density plasma. Flipped III-N/GaN samples can be directly deposited in this way. However, future work remains to the release of the III-N/GaN/Diamond film from the temporary SOG handle to create free-standing diamond. At present, this process is non-trivial since the CVD diamond overgrows around the edges, requiring laser dicing, careful wet or dry etching process to homogeneously remove the Si to evenly distribute the accumulated thermal stresses in the diamond and III-N/GaN; a release process far beyond the scope of this study. While the focus of this study is on the holder to mitigate III-N/GaN damage, other more expensive modifications can be cost-effectively investigated using modelling, in particular improving large area MP-CVD on GaN-on-Si wafers, a goal which once achieved will rapidly accelerate the adoption of diamond into the growing semiconductor industry.

### CRedit authorship contribution statement

**Jerome A. Cuenca:** Writing – review & editing, Writing – original draft, Visualization, Validation, Software, Methodology, Investigation, Formal analysis, Data curation, Conceptualization. **Ali Al-Moathin:**

Resources, Investigation. **Menno J. Kappers:** Resources. **Soumen Mandal:** Resources. **Martin Kuball:** Supervision. **Rachel A. Oliver:** Supervision, Resources. **Chong Li:** Supervision. **Oliver A. Williams:** Writing – review & editing, Supervision, Funding acquisition.

### Declaration of competing interest

The authors declare that they have no known competing financial interests or personal relationships that could have appeared to influence the work reported in this paper.

### Acknowledgements

This project has been supported by the Engineering and Physical Sciences Research Council (EPSRC), United Kingdom under the “GaN-DaMe” program grant (EP/P00945X/1), the EPSRC National Epitaxy Facility, United Kingdom (EP/X015300/1) and the Innovate UK funded “CSconnected” Strength in Places Fund (107134). Special thanks are given to Scott Cook and Lee Wescombe at Cardiff University for workshop manufacturing. Experimental data for this publication, including access details, can be found in the Cardiff University Research Data Repository at <https://doi.org/10.17035/cardiff.28937441.v1>.

### References

- [1] L. Sang, Diamond as the heat spreader for the thermal dissipation of GaN-based electronic devices, *Funct. Diam.* 1 (1) (2021) 174–188, <http://dx.doi.org/10.1080/26941112.2021.1980356>, URL <https://www.tandfonline.com/doi/full/10.1080/26941112.2021.1980356>.
- [2] O.A. Williams, S. Mandal, J.A. Cuenca, Heterogeneous integration of diamond, *Accounts Mater. Res.* 5 (10) (2024) 1172–1180, <http://dx.doi.org/10.1021/accounts.4c00126>, URL <https://pubs.acs.org/doi/10.1021/accounts.4c00126>.
- [3] A. Kobayashi, H. Tomiyama, Y. Ohno, Y. Shimizu, Y. Nagai, N. Shigekawa, J. Liang, Room-temperature bonding of GaN and diamond via a SiC layer, *Funct. Diam.* 2 (1) (2022) 142–150, <http://dx.doi.org/10.1080/26941112.2022.2145508>, URL <https://www.tandfonline.com/doi/full/10.1080/26941112.2022.2145508>.
- [4] J. Liang, A. Kobayashi, Y. Shimizu, Y. Ohno, S.-W. Kim, K. Koyama, M. Kasu, Y. Nagai, N. Shigekawa, Fabrication of GaN/diamond heterointerface and interfacial chemical bonding state for highly efficient device design, *Adv. Mater.* 33 (43) (2021) 1–13, <http://dx.doi.org/10.1002/adma.202104564>, URL <https://onlinelibrary.wiley.com/doi/10.1002/adma.202104564>.
- [5] T. Matsumae, S. Okita, S. Fukumoto, M. Hayase, Y. Kurashima, H. Takagi, Simple low-temperature GaN/diamond bonding process with an atomically thin intermediate layer, *ACS Appl. Nano Mater.* 6 (15) (2023) 14076–14082, <http://dx.doi.org/10.1021/acsanm.3c02002>, URL <https://pubs.acs.org/doi/10.1021/acsanm.3c02002>.
- [6] B. Hájek, V. Kohout, V. Flenr, Note on thermodynamic instability of  $M_4C_3$ -type carbides of gallium group metals, *Monatsh. Chem. - Chem. Mon.* 117 (10) (1986) 1157–1164, <http://dx.doi.org/10.1007/BF00811328>, URL <http://link.springer.com/10.1007/BF00811328>.
- [7] T. Ižák, V. Jirásek, G. Vanko, J. Dzuba, A. Kromka, Temperature-dependent stress in diamond-coated AlGaIn/GaN heterostructures, *Mater. Des.* 106 (2016) 305–312, <http://dx.doi.org/10.1016/j.matdes.2016.06.006>, URL <https://linkinghub.elsevier.com/retrieve/pii/S0264127516307572>.
- [8] J.A. Cuenca, M.D. Smith, D.E. Field, F. C.P. Massabuau, S. Mandal, J. Pomeroy, D.J. Wallis, R.A. Oliver, I. Thayne, M. Kuball, O.A. Williams, Thermal stress modelling of diamond on GaN/III-Nitride membranes, *Carbon* 174 (2021) 647–661, <http://dx.doi.org/10.1016/j.carbon.2020.11.067>, URL <https://linkinghub.elsevier.com/retrieve/pii/S0008622320311465>.
- [9] D.E. Field, J.A. Cuenca, M. Smith, S.M. Fairclough, F.C. Massabuau, J.W. Pomeroy, O. Williams, R.A. Oliver, I. Thayne, M. Kuball, Crystalline interlayers for reducing the effective thermal boundary resistance in GaN-on-diamond, *ACS Appl. Mater. Interfaces* 12 (48) (2020) 54138–54145, <http://dx.doi.org/10.1021/acsami.0c10129>, URL <https://pubs.acs.org/doi/10.1021/acsami.0c10129>.
- [10] M. Malakoutian, D.E. Field, N.J. Hines, S. Pasayat, S. Graham, M. Kuball, S. Chowdhury, Record-low thermal boundary resistance in GaN-on-diamond and GaN-on-SiC for enabling radiofrequency device cooling, *ACS Appl. Mater. Interfaces* 13 (50) (2021) 60553–60560, <http://dx.doi.org/10.1021/acsami.1c13833>, URL <https://pubs.acs.org/doi/10.1021/acsami.1c13833>.
- [11] M.D. Smith, J.A. Cuenca, D.E. Field, Y.-c. Fu, C. Yuan, F. Massabuau, S. Mandal, J.W. Pomeroy, R.A. Oliver, M.J. Uren, K. Elgaid, O.A. Williams, I. Thayne, M. Kuball, GaN-on-diamond technology platform: Bonding-free membrane manufacturing process, *AIP Adv.* 10 (3) (2020) 1–6, <http://dx.doi.org/10.1063/1.5129229>, URL <https://pubs.aip.org/adv/article/10/3/035306/1037541>.

- [12] D. Koleske, A. Wickenden, R. Henry, J. Culbertson, M. Twigg, GaN decomposition in H<sub>2</sub> and N<sub>2</sub> at MOVPE temperatures and pressures, *J. Cryst. Growth* 223 (4) (2001) 466–483, [http://dx.doi.org/10.1016/S0022-0248\(01\)00617-0](http://dx.doi.org/10.1016/S0022-0248(01)00617-0), URL <https://linkinghub.elsevier.com/retrieve/pii/S0022024801006170>.
- [13] Y. Morimoto, Few characteristics of epitaxial GaN—Etching and thermal decomposition, *J. Electrochem. Soc.* 121 (10) (1974) 1383, <http://dx.doi.org/10.1149/1.2401694>, URL <https://iopscience.iop.org/article/10.1149/1.2401694>.
- [14] A. Koukitsu, M. Mayumi, Y. Kumagai, Surface polarity dependence of decomposition and growth of GaN studied using in situ gravimetric monitoring, *J. Cryst. Growth* 246 (3–4) (2002) 230–236, [http://dx.doi.org/10.1016/S0022-0248\(02\)01746-3](http://dx.doi.org/10.1016/S0022-0248(02)01746-3), URL <https://linkinghub.elsevier.com/retrieve/pii/S0022024802017463>.
- [15] A. Pisch, R. Schmid-Fetzer, In situ decomposition study of GaN thin films, *J. Cryst. Growth* 187 (3–4) (1998) 329–332, [http://dx.doi.org/10.1016/S0022-0248\(98\)00006-2](http://dx.doi.org/10.1016/S0022-0248(98)00006-2), URL <https://linkinghub.elsevier.com/retrieve/pii/S0022024898000062>.
- [16] W. Fathallah, T. Boufaden, B. El Jani, Analysis of GaN decomposition in an atmospheric MOVPE vertical reactor, *Phys. Status Solidi C* 4 (1) (2007) 145–149, <http://dx.doi.org/10.1002/pssc.200673509>, URL <https://onlinelibrary.wiley.com/doi/10.1002/pssc.200673509>.
- [17] Z. Hao, K. Huang, K. Deng, F. Sun, J. Liu, L. Chen, S. Mandal, O.A. Williams, C. Li, X. Wang, J. Wei, Synthesis of nano-diamond film on GaN surface with low thermal boundary resistance and high thermal conductivity, *Carbon* 229 (2024) 119491, <http://dx.doi.org/10.1016/j.carbon.2024.119491>, URL <https://linkinghub.elsevier.com/retrieve/pii/S0008622324007103>.
- [18] G. Ma, Y. Wang, R. Xia, B. Meng, S. Yuan, B. Zhou, C. Yuan, Modulating microstructure and thermal properties of diamond/SiNx/GaN multilayer structure by diamond growth temperature, *Diam. Relat. Mater.* 141 (2024) 110717, <http://dx.doi.org/10.1016/j.diamond.2023.110717>, URL <https://linkinghub.elsevier.com/retrieve/pii/S0925963523010427>.
- [19] A. Gicquel, K. Hassouni, F. Silva, J. Achard, CVD diamond films: from growth to applications, *Curr. Appl. Phys.* 1 (6) (2001) 479–496, [http://dx.doi.org/10.1016/S1567-1739\(01\)00061-X](http://dx.doi.org/10.1016/S1567-1739(01)00061-X), URL <https://linkinghub.elsevier.com/retrieve/pii/S156717390100061X>.
- [20] O. Williams, Nanocrystalline diamond, *Diam. Relat. Mater.* 20 (5–6) (2011) 621–640, <http://dx.doi.org/10.1016/j.diamond.2011.02.015>, URL <https://linkinghub.elsevier.com/retrieve/pii/S0925963511000835>.
- [21] Y. Zhang, D. Zhang, L. Zhang, B. Yang, Z. Gan, The etching mechanisms of diamond, graphite, and amorphous carbon by hydrogen plasma: A reactive molecular dynamics study, *Adv. Theory Simulations* 6 (11) (2023) 1–7, <http://dx.doi.org/10.1002/ads.202300371>, URL <https://onlinelibrary.wiley.com/doi/10.1002/ads.202300371>.
- [22] K. Hassouni, T.A. Grotjohn, A. Gicquel, Self-consistent microwave field and plasma discharge simulations for a moderate pressure hydrogen discharge reactor, *J. Appl. Phys.* 86 (1) (1999) 134–151, <http://dx.doi.org/10.1063/1.370710>, URL <https://pubs.aip.org/jap/article/86/1/134/490075>.
- [23] A. Gicquel, M. Chenevier, K. Hassouni, A. Tserepi, M. Dubus, Validation of actinometry for estimating relative hydrogen atom densities and electron energy evolution in plasma assisted diamond deposition reactors, *J. Appl. Phys.* 83 (12) (1998) 7504–7521, <http://dx.doi.org/10.1063/1.367514>, URL <https://pubs.aip.org/jap/article/83/12/7504/180238>.
- [24] M. Fünér, C. Wild, P. Koidl, Numerical simulations of microwave plasma reactors for diamond CVD, *Surf. Coatings Technol.* 74–75 (1995) 221–226, [http://dx.doi.org/10.1016/0257-8972\(95\)08232-8](http://dx.doi.org/10.1016/0257-8972(95)08232-8), URL <https://linkinghub.elsevier.com/retrieve/pii/0257897295082328>.
- [25] H. Yamada, A. Chayahara, Y. Mokuno, Y. Soda, Y. Horino, N. Fujimori, Modeling and numerical analyses of microwave plasmas for optimizations of a reactor design and its operating conditions, *Diam. Relat. Mater.* 14 (11–12) (2005) 1776–1779, <http://dx.doi.org/10.1016/j.diamond.2005.06.037>, URL <https://linkinghub.elsevier.com/retrieve/pii/S0925963505002621>.
- [26] H. Yamada, A. Chayahara, Y. Mokuno, Simplified description of microwave plasma discharge for chemical vapor deposition of diamond, *J. Appl. Phys.* 101 (6) (2007) <http://dx.doi.org/10.1063/1.2711811>, URL <https://pubs.aip.org/jap/article/101/6/063302/1028065>.
- [27] H. Yamada, A. Chayahara, Y. Mokuno, S. Shikata, Numerical microwave plasma discharge study for the growth of large single-crystal diamond, *Diam. Relat. Mater.* 54 (1) (2015) 9–14, <http://dx.doi.org/10.1016/j.diamond.2014.11.005>, URL <https://linkinghub.elsevier.com/retrieve/pii/S0925963514002131>.
- [28] J.A. Cuenca, S. Mandal, E.L. Thomas, O.A. Williams, Microwave plasma modelling in clamshell chemical vapour deposition diamond reactors, *Diam. Relat. Mater.* 124 (2022) 108917, <http://dx.doi.org/10.1016/j.diamond.2022.108917>, URL <https://linkinghub.elsevier.com/retrieve/pii/S0925963522000991>.
- [29] M. Fünér, C. Wild, P. Koidl, Simulation and development of optimized microwave plasma reactors for diamond deposition, *Surf. Coatings Technol.* 116–119 (1999) 853–862, [http://dx.doi.org/10.1016/S0257-8972\(99\)00233-9](http://dx.doi.org/10.1016/S0257-8972(99)00233-9), URL <https://linkinghub.elsevier.com/retrieve/pii/S0257897299002339>.
- [30] F. Silva, K. Hassouni, X. Bonnin, A. Gicquel, Microwave engineering of plasma-assisted CVD reactors for diamond deposition, *J. Phys.: Condens. Matter.* 21 (36) (2009) 364202, <http://dx.doi.org/10.1088/0953-8984/21/36/364202>, URL <https://iopscience.iop.org/article/10.1088/0953-8984/21/36/364202>.
- [31] Z. Yang, Z. Guo, K. An, Y. Liu, Y. Wang, J. Wei, J. Liu, L. Chen, X. Ouyang, C. Li, Effect of argon addition on CH<sub>4</sub>-H<sub>2</sub> microwave plasma: Self-consistent simulation and nanodiamond coating deposition, *Surf. Coatings Technol.* 490 (2024) 131165, <http://dx.doi.org/10.1016/j.surfcoat.2024.131165>, URL <https://linkinghub.elsevier.com/retrieve/pii/S0257897224007965>.
- [32] E.J.D. Mahoney, B.S. Truscott, S. Mushtaq, M.N.R. Ashfold, Y.A. Mankelevich, Spatially resolved optical emission and modeling studies of microwave-activated hydrogen plasmas operating under conditions relevant for diamond chemical vapor deposition, *J. Phys. Chem. A* 122 (42) (2018) 8286–8300, <http://dx.doi.org/10.1021/acs.jpca.8b07491>, URL <https://pubs.acs.org/doi/10.1021/acs.jpca.8b07491>.
- [33] M.N. Ashfold, Y.A. Mankelevich, Two-dimensional modeling of diamond growth by microwave plasma activated chemical vapor deposition: Effects of pressure, absorbed power and the beneficial role of nitrogen on diamond growth, *Diam. Relat. Mater.* 137 (2023) 110097, <http://dx.doi.org/10.1016/j.diamond.2023.110097>, URL <https://linkinghub.elsevier.com/retrieve/pii/S0925963523004223>.
- [34] J.A. Cuenca, W. Leigh, E.L. Thomas, S. Mandal, O.A. Williams, Modelling deposition uniformity in microwave plasma CVD diamond over 2" si wafers, in: 2022 Asia-Pacific Microw. Conf., November, IEEE, Yokohama, 2022, pp. 656–658, <http://dx.doi.org/10.23919/APMC55665.2022.9999754>, URL <https://ieeexplore.ieee.org/document/9999754>.
- [35] V. Sedov, A. Martyanov, A. Altakhov, A. Popovich, M. Shevchenko, S. Savin, E. Zavedev, M. Zhanavskina, A. Sinogeykin, V. Ralchenko, V. Konov, Effect of substrate holder design on stress and uniformity of large-area polycrystalline diamond films grown by microwave plasma-assisted CVD, *Coatings* 10 (10) (2020) 939, <http://dx.doi.org/10.3390/coatings10100939>, URL <https://www.mdpi.com/2079-6412/10/10/939>.
- [36] B. Yang, Q. Shen, Z. Gan, S. Liu, Analysis of improving the edge quality and growth rate of single-crystal diamond growth using a substrate holder, *CrystEngComm* 21 (43) (2019) 6574–6584, <http://dx.doi.org/10.1039/C9CE01402K>, URL <https://xlink.rsc.org/?DOI=C9CE01402K>.
- [37] J. Weng, F. Liu, Z. Wang, N. Guo, F. Fan, Z. Yang, J. Wang, H. Wang, L. Xiong, H. Zhao, J. Wang, Investigation on the preparation of large area diamond films with 150–200 mm in diameter using 915 MHz MPCVD system, *Vacuum* 217 (2023) 112543, <http://dx.doi.org/10.1016/j.vacuum.2023.112543>, URL <https://linkinghub.elsevier.com/retrieve/pii/S0042207X23007406>.
- [38] G. Wu, M.-H. Chen, J. Liao, The influence of recess depth and crystallographic orientation of seed sides on homoepitaxial growth of CVD single crystal diamonds, *Diam. Relat. Mater.* 65 (2016) 144–151, <http://dx.doi.org/10.1016/j.diamond.2016.03.011>, URL <https://linkinghub.elsevier.com/retrieve/pii/S0925963516300735>.
- [39] A. Charris, S. Nad, J. Asmussen, Exploring constant substrate temperature and constant high pressure SCD growth using variable pocket holder depths, *Diam. Relat. Mater.* 76 (2017) 58–67, <http://dx.doi.org/10.1016/j.diamond.2017.04.010>, URL <https://linkinghub.elsevier.com/retrieve/pii/S0925963516307270>.
- [40] X. Zhou, P.D. Pedrow, Z. Tang, S. Bohnet, S.S. Sablani, J. Tang, Heating performance of microwave ovens powered by magnetron and solid-state generators, *Innov. Food Sci. Emerg. Technol.* 83 (2023) 103240, <http://dx.doi.org/10.1016/j.ifset.2022.103240>, URL <https://linkinghub.elsevier.com/retrieve/pii/S1466856422003253>.
- [41] G. Lombardi, K. Hassouni, G.-D. Stancu, L. Mechold, J. Röpcke, A. Gicquel, Modeling of microwave discharges of H<sub>2</sub> admixed with CH<sub>4</sub> for diamond deposition, *J. Appl. Phys.* 98 (5) (2005) <http://dx.doi.org/10.1063/1.2034646>, URL <https://pubs.aip.org/aip/jap/article-abstract/98/5/053303/292302>.
- [42] K. Hassouni, O. Leroy, S. Farhat, A. Gicquel, Modeling of H<sub>2</sub> and H<sub>2</sub>/CH<sub>4</sub> moderate-pressure microwave plasma used for diamond deposition, *Plasma Chem. Plasma Process.* 18 (3) (1998) 325–362, <http://dx.doi.org/10.1023/A:1021845402202>, URL <https://link.springer.com/article/10.1023/A:1021845402202>.
- [43] J.H. Parker, D.W. Feldman, M. Ashkin, Raman scattering by silicon and germanium, *Phys. Rev.* 155 (3) (1967) 712–714, <http://dx.doi.org/10.1103/PhysRev.155.712>, URL <https://link.aps.org/doi/10.1103/PhysRev.155.712>.
- [44] M. Kuball, Raman spectroscopy of gan, AlGaN and AlN for process and growth monitoring/control, *Surf. Interface Anal.* 31 (10) (2001) 987–999, <http://dx.doi.org/10.1002/sia.1134>, URL <https://analyticalsciencejournals.onlinelibrary.wiley.com/doi/10.1002/sia.1134>.
- [45] M. Mermoux, S. Chang, H.A. Girard, J.-C. Arnault, Raman spectroscopy study of detonation nanodiamond, *Diam. Relat. Mater.* 87 (2018) 248–260, <http://dx.doi.org/10.1016/j.diamond.2018.06.001>, URL <https://linkinghub.elsevier.com/retrieve/pii/S0925963517306969>.
- [46] J.A. Cuenca, S. Mandal, J. Stritt, X. Zheng, J. Pomeroy, M. Kuball, A. Porch, O.A. Williams, Dielectric properties of diamond using an X-band microwave split dielectric resonator, *Carbon* 221 (2024) 118860, <http://dx.doi.org/10.1016/j.carbon.2024.118860>, URL <https://linkinghub.elsevier.com/retrieve/pii/S0008622324000770>.
- [47] S. Praver, R.J. Nemanich, Raman spectroscopy of diamond and doped diamond, *Philos. Trans. R. Soc. Lond. Ser. A Math. Phys. Eng. Sci.* 362 (1824) (2004) 2537–2565, <http://dx.doi.org/10.1098/rsta.2004.1451>, URL <https://royalsocietypublishing.org/doi/10.1098/rsta.2004.1451>.

- [48] K.A. Snail, C.M. Marks, In situ diamond growth rate measurement using emission interferometry, *Appl. Phys. Lett.* 60 (25) (1992) 3135–3137, <http://dx.doi.org/10.1063/1.106747>, URL <https://pubs.aip.org/apl/article/60/25/3135/525681>.
- [49] S. Linnik, A. Gaydaychuk, Application of optical emission spectroscopy for the determination of optimal CVD diamond growth parameters in abnormal glow discharge plasma, *Vacuum* 103 (2014) 28–32, <http://dx.doi.org/10.1016/j.vacuum.2013.12.001>, URL <https://linkinghub.elsevier.com/retrieve/pii/S0042207X13003850>.
- [50] J. Su, Y. Li, Y. Liu, M. Ding, W. Tang, Revisiting the gas flow rate effect on diamond films deposition with a new dome-shaped cavity type microwave plasma CVD reactor, *Diam. Relat. Mater.* 73 (2017) 99–104, <http://dx.doi.org/10.1016/j.diamond.2016.07.014>, URL <https://linkinghub.elsevier.com/retrieve/pii/S0925963516301674>.
- [51] C. Yuan, R. Hanus, S. Graham, A review of thermoreflectance techniques for characterizing wide bandgap semiconductors' thermal properties and devices' temperatures, *J. Appl. Phys.* 132 (22) (2022) <http://dx.doi.org/10.1063/5.0122200>, URL <https://pubs.aip.org/jap/article/132/22/220701/2837816>.
- [52] Y.-H. Yeh, K.-M. Chen, Y.-H. Wu, Y.-C. Hsu, W.-I. Lee, Hydrogen etching on the surface of GaN for producing patterned structures, *J. Cryst. Growth* 314 (1) (2011) 9–12, <http://dx.doi.org/10.1016/j.jcrysgro.2010.10.063>, URL <https://linkinghub.elsevier.com/retrieve/pii/S0022024810007931>.
- [53] W.G. Leigh, J.A. Cuenca, E.L. Thomas, S. Mandal, O.A. Williams, Mapping the effect of substrate temperature inhomogeneity during microwave plasma-enhanced chemical vapour deposition nanocrystalline diamond growth, *Carbon* 201 (2023) 328–337, <http://dx.doi.org/10.1016/j.carbon.2022.09.036>, URL <https://linkinghub.elsevier.com/retrieve/pii/S0008622322007606>.
- [54] H. Kambalathmana, A. Flatae, L. Hunold, F. Sledz, J. Müller, M. Hepp, P. Schmuki, M. Killian, S. Lagomarsino, N. Gelli, S. Sciortino, L. Giuntini, E. Wörner, C. Wild, B. Butz, M. Agio, Optical properties of silicon-implanted polycrystalline diamond membranes, *Carbon* 174 (2021) 295–304, <http://dx.doi.org/10.1016/j.carbon.2020.12.031>, URL <https://linkinghub.elsevier.com/retrieve/pii/S0008622320312082>.
- [55] H. Chen, H. Fu, X. Huang, X. Zhang, T.-H. Yang, J.A. Montes, I. Baranowski, Y. Zhao, Low loss GaN waveguides at the visible spectral wavelengths for integrated photonics applications, *Opt. Express* 25 (25) (2017) 31758, <http://dx.doi.org/10.1364/OE.25.031758>, URL <https://opg.optica.org/abstract.cfm?URI=oe-25-25-31758>.